Orientation and rate dependence in high strain-rate compression of single-crystal silicon

R. F. Smith,[1] R. W. Minich,[1] R. E. Rudd,[1] J. H. Eggert,[1] C. A. Bolme,[2] S. L. Brygoo,[3] A. M. Jones,[1,*] and G. W. Collins[1]

[1]*Lawrence Livermore National Laboratory, P.O. Box 808, Livermore, California 94550, USA*

[2]*Los Alamos National Laboratory, P.O. Box 1663, Los Alamos, New Mexico 87545, USA*

[3]*CEA, DAM, DIF, F-91297 Arpajon, France*

(Received 6 August 2012; published 17 December 2012)

High strain-rate ($\dot{\varepsilon} \sim 10^6 - 10^9\ \mathrm{s}^{-1}$) compression of single crystal Si reveals strong orientation- and rate-dependent precursor stresses. At these high compression rates, the peak elastic stress, $\sigma_{\mathrm{E\_Peak}}$, for Si [100], [110], and [111] exceeds twice the Hugoniot elastic limit. Near the loading surface, the rate at which Si evolves from uniaxial compression to a three-dimensional relaxed state is exponentially dependent on $\sigma_{\mathrm{E\_Peak}}$ and independent of initial crystal orientation. At later times, the high elastic wave speed results in a temporal decoupling of the elastic precursor from the main inelastic wave. A rapid high-$\dot{\varepsilon}$ increase in the measured elastic stress at the onset of inelastic deformation is consistent with a transition from dislocation flow mediated by thermal activation to a phonon drag regime.

DOI: 10.1103/PhysRevB.86.245204 PACS number(s): 61.72.uf, 62.20.F−, 62.20.D−

I. INTRODUCTION

Understanding the kinetics of high strain-rate compression is of fundamental importance in the study of many physical phenomena ranging from high-speed collisions[1] to inertial confinement fusion implosions.[2] In such processes, the time-dependent stress-strain ($\vec{\sigma}(t) - \vec{\varepsilon}(t)$) response is determined by the dynamics of dislocation creation and flow and is a complex function of time, sample purity, microstructure,[3–8] temperature,[9] internal stresses, and loading rate.[10] Despite decades of research, there remains a lack of quantitative experimental data on the kinetics of dislocation formation and flow in materials undergoing high strain-rate deformation. Data at very high strain rates ($\dot{\varepsilon} > 10^6\ \mathrm{s}^{-1}$), such as presented here, are important to improve widely used dislocation kinetic models, which, while successful at describing low strain-rate plastic deformation,[11] fail at high strain rates without the inclusion of additional source mechanisms.[12]

Silicon is an ideal material to study the dynamics of high strain-rate deformation due to the availability of high purity, low dislocation density ($<10^5\ \mathrm{cm}^{-2}$), and well-orientated single crystals. Quasistatic compression studies on silicon,[13] which under ambient conditions has a diamond crystal structure, have revealed several pressure-induced polymorphic phase transformations between ∼12–18 GPa. Uniaxial shock compression through flyer-plate impact on single crystal samples have provided measurements on the stresses associated with elastic-plastic deformation and the onset of a phase transformation at ∼13–16 GPa.[3–6] As is characteristic of ceramic materials, Si exhibits high elastic stresses and a complete loss of shear stress upon the onset of plastic deformation.[3,5] The deformation mechanisms in Si can vary greatly depending on the temperature, strain rate, and nature of compression. Under an applied stress at room temperature, Si often deforms through brittle failure due to the characteristically low dislocation flux. At elevated temperatures (∼420 K), there is a brittle to ductile transition in Si due to an increased dislocation mobility facilitating plastic flow.[14] Although the temperature rise in our experiments is estimated to be <75 K at 15 GPa,[15] well within the brittle regime, inertial confinement associated with the uniaxial compression experiments reported here is expected to suppress the onset of brittle fracture, enhancing ductility.[16,17]

In this paper, we use a recently developed laser-driven ramp-wave-loading (RWL) technique[18,19] to uniaxially compress single-crystal Si samples to a peak longitudinal stress of 50 GPa over several to tens of nanoseconds ($\dot{\varepsilon} \sim 10^6 - 10^8\ \mathrm{s}^{-1}$). This variability in $\dot{\varepsilon}$ permits a systematic study of the orientation- and time-dependence of stresses associated with elastic deformation and shear-stress relaxation. To access higher strain-rates, we also employ laser-driven shock compression ($\dot{\varepsilon} \sim 10^9\ \mathrm{s}^{-1}$).

The paper has the following layout. Section II describes the experimental method. Section III reports on four separate measurements: (a) anisotropic elastic compression, (b) inelastic stress relaxation, (c) Lagrangian sound speed measurements, and (d) high strain-rate response. In Sec. IV, we show the output of a rate-dependent plasticity model. Conclusions are reported in Sec. V.

II. EXPERIMENTAL METHOD

The RWL data were obtained on the Omega and Janus laser facilities. Omega is a 60-beam 40 kJ Nd glass laser system producing frequency-tripled 351-nm radiation located at the Laboratory of Laser Energetics [LLE] in New York.[20] The Janus laser is a two-beam facility that delivers 1 kJ of laser energy at 527 nm and is based at the Lawrence Livermore National Laboratory in California. The target design for the Janus RWL experiments is shown in Fig. 1(a). The target consists of a 100-μm polyimide [$C_{22}H_{10}N_2O_5$] foil followed by a 150–350-μm vacuum gap and a 40–340-μm-thick single crystal Si target. The polyimide is irradiated for 4-ns by the 1-mm-square spatially planar 527-nm Janus laser (300 J), generating an ablatively driven shock. After shock breakout from the rear surface, the polyimide rarefies across the vacuum gap, monotonically loads up against the Si sample, and launches a temporally smooth ramp-compression wave. Due to the planar inertially confined nature of the ramp drive, our samples are in a state of uniaxial strain. By changing the vacuum gap size and laser intensity, the compression rate is varied by a factor of fifty ($\dot{\varepsilon} \sim 10^6 - 5 \times 10^7\ \mathrm{s}^{-1}$).

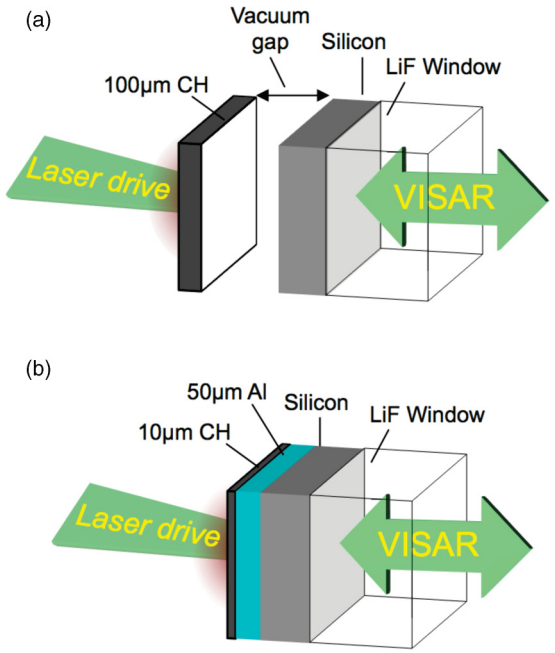

FIG. 1. (Color online) (a) Target design form laser ramp wave-loading experiments on the Janus laser. (b) Target design for laser-driven shock-compression experiments on the Janus laser. For some shots a LiF window was used that was glued onto the Si. The estimated glue layer thickness at the Al/Si and Si/LiF interfaces was 3 μm.

The silicon, supplied by Silicon Quest Ca., was n doped (Phosphorus) and had resistivities of >5000, >2000, and $>4000\ \Omega\ \mathrm{cm}^{-1}$ for [111], [110], and [100], respectively, with corresponding dopant densities of $>8.2\times10^{11}$, 2.1×10^{12}, and $\sim1\times10^{12}\ \mathrm{cm}^{-3}$. The orientation of the crystals where determined to be $0\pm0.5^\circ$ for Si [100], $0\pm0.5^\circ$ for Si [110], and $4\pm0.5^\circ$ off Si [111]. Transmission electron microscopy (TEM) of our Si samples found no dislocations or dislocation sources in the bulk and sets an upper limit for the initial dislocation density of $1.3\times10^5\ \mathrm{cm}^{-2}$.

Experiments were also conducted where Si samples were subjected to 30 GPa shock compression, and the deformation response as a function of sample thickness (10 to 340 μm) was recorded. The target geometry for the shock-compression experiments is shown in Fig. 1(b). Here a 6-ns-square laser pulse from the Janus laser with 200 J of energy directly ablates the 10-μm CH layer backed by 50 μm of Al. This setup ensures a steady shock with $\sim$4 ns duration was launched into the Si sample.[21] In some cases, LiF windows are used to reduce interface wave interactions.

A slightly modified target design is employed for RWL experiments on the Omega laser. The target consists of a 180-μm 12% Br-doped plastic foil [C_4H_3Br] separated by a 400-μm vacuum gap from a single-crystal Si stepped target [Fig. 2(a)]. The target is driven over a circular area 2 mm in diameter by x radiation from an Au hohlraum, generating an ablatively driven shock.[22] After shock breakout from the rear surface, the Br-CH unloads across the vacuum gap, loads up against the Si, and launches a smoothly increasing ramp-compression wave. The high spatial planarity associated with the x-ray drive from the Omega hohlraum enables different thicknesses of Si to be compressed with a common

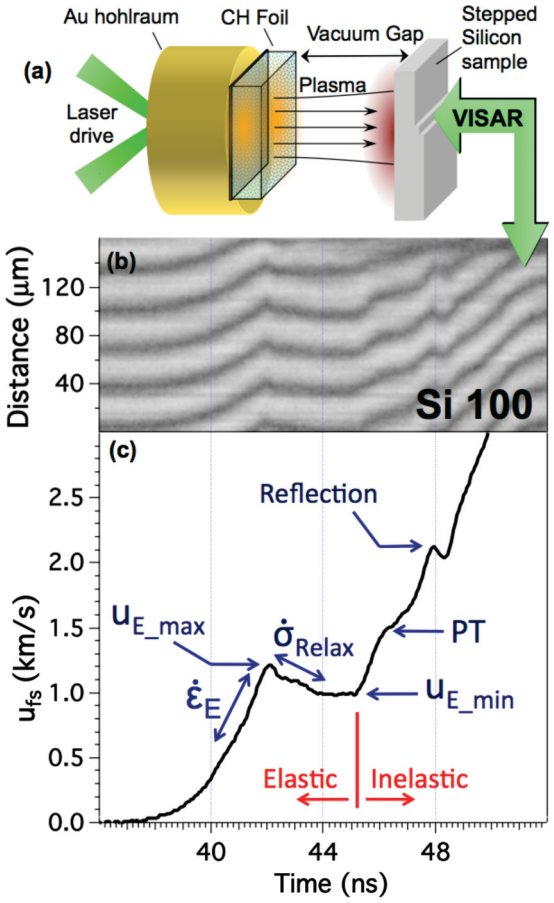

FIG. 2. (Color online) (a) Target design for laser-driven ramp compression of Si on the Omega laser. (b) The VISAR streak camera record of the time-resolved Si/vacuum interface velocity for a 70-μm-thick Si [100] target (Omega shot #47294). (c) The extracted free-surface velocity, u_{fs}, versus time. We observe an elastic precursor with a compressive strain rate $\dot{\varepsilon}_E$ and a peak velocity u_{E_Max}. After u_{E_Max}, there is a velocity pullback with an associated stress relaxation rate, $\dot{\sigma}_{Relax}$. At a $u_{fs}\sim1.43$ km/s, there is a "ramped" plateau, which is a signature of the drop in the sound speed consistent with the onset of a phase transformation (Ref. 4). The pullback in the u_{fs} profile at $\sim$2.1 km/s is caused by interaction of the incoming ramp wave and the reflected elastic wave due to the impedance mismatch at the Si/vacuum interface. Our analysis is consistent with the onset of significant plastic flow initiating at u_{E_min}.

compression history to peak-stress states of 50 GPa.[19] The Si step samples are fabricated through lithographic etching from commercially available 4-inch-diameter Si wafers to thicknesses of $\sim30/70/90$ μm. Interferometry is used to determine that the surface roughness is <0.03 μm, thickness gradients were $<1\%$, and step heights are known to <0.1 μm. For all experiments, the time history of the transmitted compression wave was recorded by measuring the Si/vacuum free-surface velocity, $u_{fs}(t)$, or Si/LiF interface velocity, $u(t)$, with a line-imaging velocity interferometer (VISAR: velocity interferometer system for any reflector).[23] The VISAR detects the Doppler shift of reflected laser light (532 nm) to record the time history of the surface velocity. Two VISARs with different velocity sensitivities were used to provide redundant data and resolve any ambiguities associated with sharp velocity

jumps that exceed the time response of the system. The velocity sensitivity of the interference fringes recorded by the VISAR is controlled by inserting different lengths of fused silica etalons in one leg of the interferometer to alter the optical delay in that leg. In our experiments, we used etalon lengths of 45.1006 and 60.083 mm to produce velocity-per-fringe (VPF) constants of 1.105 and 0.829 km/s.

Figure 2(b) shows a typical streak camera output of the VISAR for a 70-μm-thick Si [100] target along with the extracted $u_{\rm fs}(t)$ profile [Fig. 2(c), Omega shot #47294]. Here, the temporal resolution is 50 ps, the velocity per fringe is 1.105 km s^{-1}, and the fringe position is determined to within 2% of a fringe period. The standard interpretation of the wave profile data in Fig. 2(c) is that in the precursor wave there is an initial period of (truly) elastic deformation until the dynamic shear stress reaches a level sufficiently high for multiplication or nucleation of defects (e.g., dislocations) to occur. There is an ensuing period of incubation until the defect population is sufficient to support the requisite plastic strain rate, and then (at $u_{\rm E\_max}$) the shear stress drops in a plastic (or possibly viscoplastic) relaxation. In Fig. 2(c), this rapid stress-relaxation rate, $\dot{\sigma}_{\rm Relax}$, is followed by a plateau with a velocity consistent with the steady-state Hugoniot elastic limit (HEL) values measured by Gust and Royce.[4] The elastic precursor wave, traveling at the longitudinal sound speed, separates in time from the slower moving (bulk sound speed) inelastic wave.

III. REVIEW OF EXPERIMENTAL DATA

In the following section, we report on a number of experiments designed to study the time and orientation dependence of high strain-rate deformation in single crystal silicon.

A. Anisotropic elastic response

In our experiments, the transmitted compression wave profile is measured as a velocity at the Si-free surface [$u_{\rm fs}(t)$, Fig. 2(c)] or Si/LiF interface ($u(t)$). To relate $u_{\rm fs}$ to an equivalent elastic stress within the bulk Si, we use the reported second- and third-order elastic constants for Si to calculate the following σ_x–ρ relationships for each orientation:[24] $\sigma_x = -196.49 + 97.5\rho - 5.65\rho^2$ (Si [100]); $\sigma_x = -24.78 - 63.05\rho + 31.62\rho^2$ (Si [110]); $\sigma_x = -113.69 + 10.26\rho + 16.54\rho^2$ (Si [111]) GPa with density ρ in g/cm^3. σ_x refers to the longitudinal stress in the loading direction. The Lagrangian sound speed, $C_{\rm L}$, and the free-surface velocity are then related to σ_x by $C_{\rm L} = \frac{\rho}{\rho_0}(\frac{\delta\sigma_x}{\delta\rho})^{1/2}$ and $u_{\rm fs} = \frac{2}{\rho_0}\int_0^{\sigma_x}\frac{d\sigma_x}{C_{\rm L}}$. For samples with LiF windows, the σ_x was calculated from the Si/LiF velocity profile using the relationships reported in Ref. 5.

Figure 3(a) shows the elastic stress, $\sigma_{\rm E}$, as a function of sample thickness for Si [100]. The green circle and red square symbols represent our laser ramp- and shock-compression experiments, respectively. Here $\sigma_{\rm E}$ is calculated at the precursor pullback velocity [$u_{\rm E\_min}$ in Fig. 2(c)]. The extent of the positive error bars represents the value of $\sigma_{\rm E}$ if the peak precursor velocity is used [$u_{\rm E\_max}$ in Fig. 2(c)]. The errors in stress, due to uncertainty in the determination of $u_{\rm E}$, are $\sim\pm$0.3 GPa. This value takes into account the inherent accuracy of the measurement and uncertainties due to drive nonuniformity. Also shown are shock-compression data in the 1–10 mm range from Goto,[3] Gust,[4] and Turneaure.[5] We observe a time-dependent decay in the elastic stress. This is consistent with observations of wave behavior in ductile metals, in which the peak elastic stress decays continuously from a maximum value at the surface which experiences the initial compressive load (loading surface) towards an

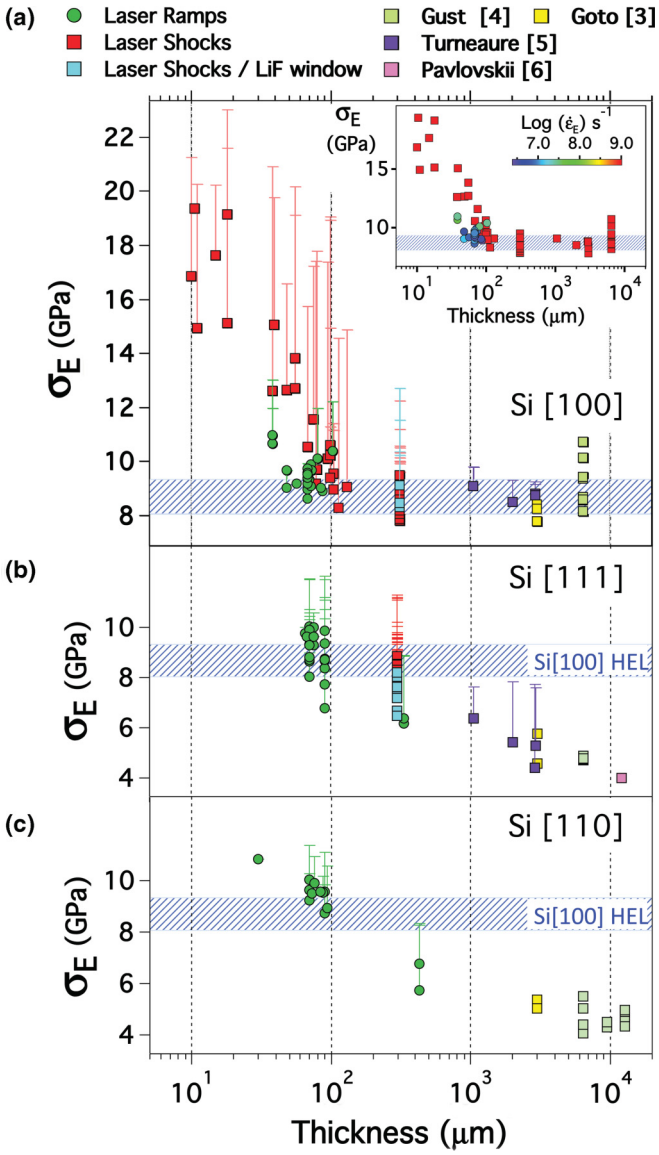

FIG. 3. (Color online) (a) Elastic stress versus sample thickness for Si [100]. The elastic stress $\sigma_{\rm E}$ is calculated at the precursor pullback velocity ($u_{\rm E\_min}$ in Fig. 1). The extent of the positive error bars signifies the value for the peak elastic stress ($u_{\rm E\_max}$ in Fig. 1). At thicknesses greater than 100 μm, the elastic precursor has reached a steady-state HEL. The average value (plus uncertainty) for the Si [100] HEL is shown as the shaded blue area. Shown as an inset are the $\sigma_{\rm E}$-thickness data with the color scale representing the strain rate of compression in the elastic precursor, $\dot{\varepsilon}_E$. (b), (c) The $\sigma_{\rm E}$-thickness values for Si [110] and [111]. The anisotropic response of silicon is evident as the elastic stress falls far below the [100] HEL, and the limiting value is not reached for these orientations until 10 mm of propagation or greater.

equilibrium elastic limit. The rate of elastic stress decay is determined by time-dependent plastic flow behind the elastic shock front.[10]

In our analysis, we define the longitudinal strain rate associated with compression towards the peak elastic stress [Fig. 2(c)] as

$$\dot{\varepsilon}_E = \frac{V_0}{V}\frac{du/dt}{C_L}, \tag{1}$$

where C_L is the Lagrangian sound speed, V is the volume, and u is the particle velocity. The derivation for the strain-rate expression in Eq. (1) is described in Appendix A. Correction for the wave interactions at the Si-vacuum interface is performed by considering the interaction of the oncoming ramp with the reflected release ramp.[26] The samples are sufficiently thick such that the reflected waves from the Si-vacuum interface do not reach the initial loading surface until late times. Values for C_L are determined from the sound speed analysis using stepped samples as described in Sec. III C.

Shown as an inset to Fig. 3(a) are the σ_E-thickness data with the color scale representing the strain rate of compression in the elastic precursor, $\dot{\varepsilon}_E$. For a given sample thickness, the lower $\dot{\varepsilon}$ laser-ramp data is observed to have a lower σ_E than the shock compression data. After ~100 μm of propagation, the elastic stress has decayed to the HEL for all values of $\dot{\varepsilon}_E$. C_L associated with elastic compression in Si [100] is ~8.5 km/s [Sec. III C], so decay toward the HEL yield surface occurs in $\leqslant$11.7 ns. By contrast, for shock loading in pure fcc-Al, σ_E decay toward a HEL yield surface takes >4 μ-sec (>26 mm of propagation).[10]

The blue shaded area in Fig. 3 represents the average and standard deviation of the Si [100] HEL (8.69 ± 0.63 GPa) taken from samples thicknesses >100 μm. Shown in Figs. 3(b) and 3(c) are the σ_E-thickness data for Si [110] and Si [111]. Anisotropic elastic response is evident as the elastic stress continues to decay for these orientations, well below the elastic limit for Si [100], out to ~10 mm of propagation. Elastic shock speeds for Si [110] and [111] are ~9.45 km/s and ~9.6 km/s, respectively.[3] Based on the continual decay of σ_E in Figs. 3(b) and 3(c) out to thicknesses of ~10 mm, this places a lower limit on the relaxation time to the HEL yield surface as >1 μ-sec for both [110] and [111] orientations, which is more than a hundred times slower than found for the [100] orientation.

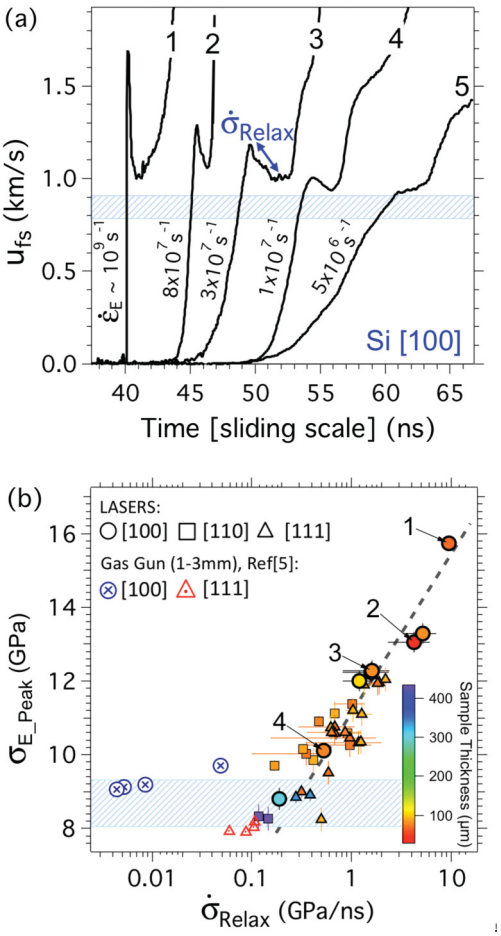

FIG. 4. (Color online) (a) $u_{fs}(t)$ traces from five separate experiments are shown artificially separated in time for clarity. These traces represent the response of 70 ± 10-μm-thick Si [100] samples compressed over a range of loading strain-rates, $\dot{\varepsilon}_E$. $\dot{\varepsilon}_E$ has a pronounced effect on the shape of the precursor with the peak elastic stress, σ_{E_Peak}, observed to increase as a function of $\dot{\varepsilon}_E$. In (b) we plot peak elastic stress versus stress relaxation rate for a range of sample thicknesses (color bar). Profiles 1–4 in (a) are labeled in (b). The stress relaxation rate is driven by the peak elastic stress state and is independent of initial crystal orientation and sample thickness. The shaded blue area represents the Si [100] HEL (average value and standard deviation) in velocity and stress space for (a) and (b), respectively.

B. Inelastic stress relaxation

Figure 4(a) shows the precursor in the $u_{fs}(t)$ profile for five different experiments on 70-μm-thick Si [100] samples with the elastic strain rates ranging from $\dot{\varepsilon}_E = 5 \times 10^6\ s^{-1}$ (trace 5) to $\sim 10^9\ s^{-1}$ (trace 1). The peak velocity of the elastic precursor is a strong function of $\dot{\varepsilon}_E$. For $\dot{\varepsilon}_E \leqslant 5 \times 10^6\ s^{-1}$, the precursor peak is consistent with the HEL value (blue shaded area). For strain-rates $\geqslant 10^7\ s^{-1}$, we observe an overshoot of the HEL followed by a rapid velocity pullback after the precursor peak with an associated stress-relaxation rate $\dot{\sigma}_{Relax}$.

In Fig. 4(b), the longitudinal stress relaxation rate, $\dot{\sigma}_{Relax}$, is shown as a function of the peak elastic stress, σ_{E_Peak} for all three orientations. Here, $\dot{\sigma}_{Relax} = \frac{(\sigma_{E\_Peak} - \sigma_{HEL})}{\Delta t}$, where Δt is the decay time from u_{E_max} to u_{HEL}. In many cases, the free-surface velocity does not fully decay to u_{HEL} after u_{E_max} due to the onset of inelastic deformation. Here, Δt is estimated through linear extrapolation of the negative du_{fs}/dt slope. Similar analysis was also applied to the shock compression data reported for 1–3 mm targets.[5] The uncertainties in $\dot{\sigma}_{Relax}$ reflect how close the data are to this assumed linear decay. Here, σ_{E_Peak} (and hence σ_{Shear}) act as a driving force for the dislocation flux, with the highest value of σ_{E_Peak} causing the most rapid stress relaxation. A fit to the data (black dashed curve) reveals a $\sigma_{E\_Peak} = 1.68^{*}\ln(\dot{\sigma}_{Relax}/a)$ relationship for $\sigma_{E\_Peak} > \sigma_{HEL}$, where $a = 0.0013$ GPa/ns. For Si [100], $\dot{\sigma}_{Relax}$ falls precipitously as $\sigma_{E\_Peak} \approx \sigma_{HEL}$. While significant crystal anisotropy is observed during elastic deformation, upon yielding, the stress-relaxation rate is observed to have the same exponential dependence on σ_E for all initial crystal orientations.

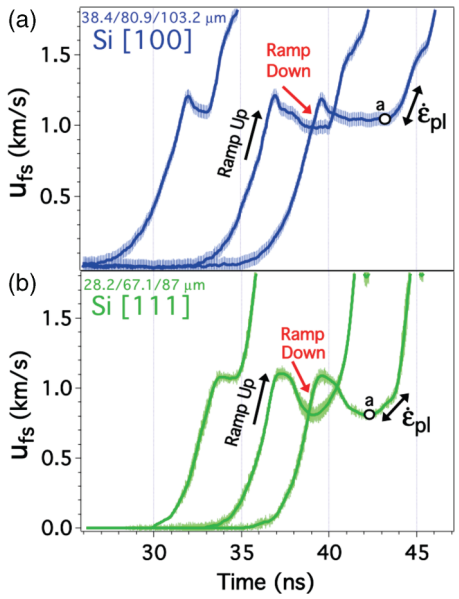

FIG. 5. (Color online) u_{fs} versus time for ramp compression of multistepped (a) Si [100] and (b) Si [111] targets at the Omega laser facility. The high spatial planarity in the drive ensures that each thickness of Si experiences the same pressure loading history. In our sound speed analysis (Fig. 6), point 'a' signifies the onset of significant plastic flow. $\dot{\varepsilon}_{pl}$ represents the strain rate at the onset of plastic flow.

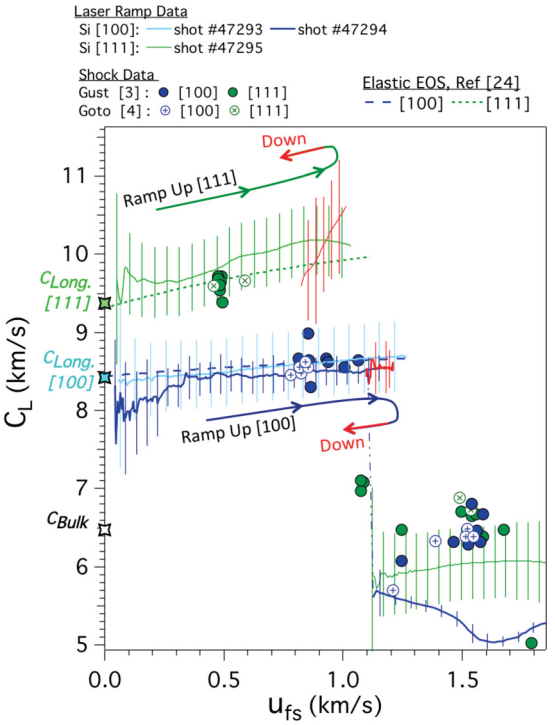

FIG. 6. (Color online) The Lagrangian sound speed as a function of free-surface velocity was calculated from the $u_{fs}(t)$ profiles in Fig. 5. Also shown are the ambient bulk and longitudinal sound speeds (star symbols; Ref. 3) and sound speed measurements from shock compression on mm-thick samples (circles; Refs. 3 and 4). The estimated elastic response for Si [100] and [111] based on elastic constants measured by McSkimin (Ref. 24) are shown as the dashed lines. After the peak of the elastic precursor there is a rapid velocity pullback (red arrows in Fig. 5). Here the Lagrangian sound speed is also consistent with an elastic sound speed for both [100] and [111] orientations. At higher values of u_{fs} there is a large drop in the material sound speed to ~5.7 km/s, which is consistent with the bulk sound speed and the onset of plastic deformation. Our data suggests the onset of significant plastic deformation is not at the precursor peak but rather at the arrival of the main compression wave (point a in Fig. 5).

Using a rate-dependent, dislocation-based continuum model of plasticity, it has been shown in Fe that under ramp-loading conditions σ_{E_Peak}, is uniquely related to $\dot{\varepsilon}_E$ due to the interplay between the loading rate and the time dependence of incipient plasticity.[10] In addition, the onset of plasticity results in shear-stress relaxation initiated at σ_{E_Peak} and at a rate proportional to σ_{E_Peak}. Those conclusions are consistent with the observations on Si reported in Fig. 4.

C. Lagrangian sound speed measurements

The high spatial planarity associated with the x-ray drive from the Omega laser allows different thicknesses of Si to be compressed with a common compression history to peak stress states of ~50 GPa.[19,22] Shown in Fig. 5 are the elastic precursors associated with ramp compression of a (a) 38.4/80.9/103-μm-thick Si [100] target and (b) a 28.2/67.1/87-μm Si [111] target. The temporal shape of velocity profiles at the precursor maximum velocity is noticeably more peaked for Si [100], which is a further signature of orientation-dependent dislocation flow. We note that there is no measureable decay of the peak elastic stress as a function of propagation thickness. This disagrees with the standard picture of elastic precursor attenuation in metals due to plastic flow behind the elastic front.[10] Recent results by Asay[25] on annealed Ta samples with very low initial dislocation density also exhibited a constant peak elastic stress (in excess of the HEL value), which showed no decay over the 2–6-mm sample thickness range. In that work, the annealed Ta samples also exhibited a strong stress relaxation immediately following the peak elastic stress. By contrast, Asay also showed that cold-rolled Ta samples, with a much higher initial dislocation density, exhibited a decay of peak elastic stress as a function of propagation thickness but an absence of a precursor velocity pullback feature.

In Fig. 6 we calculate the Lagrangian sound speed, C_L versus u_{fs} for the profiles shown in Fig. 5 by an iterative Lagrangian analysis technique, which accounts for wave interactions at the free surface.[19,26] Also shown are the calculated longitudinal and bulk sound speeds[3] (star symbols), the C_L-u_{fs} elastic response calculated from second- and third-order elastic constants (dashed lines),[24] and sound-speed measurements from shock compression on mm-thick samples (circles).[3,4] Initially the elastic precursor propagates at the longitudinal sound speed. The relatively flat C_L–u_{fs} response in the u_{fs} ~ 0−1.2 km/s range is witnessed in the $u_{fs}(t)$ profiles in Fig. 5 by the near-constant rise time toward the precursor peak for different thickness samples (i.e., the wave does not steepen strongly as a function of propagation distance). Once there is significant inelastic deformation there is a large drop in C_L from 8–10 km/s to 5–6 km/s. This drop in C_L to values comparable to the bulk sound speed is consistent with the

reported total loss of shear strength in silicon with the onset of plastic flow.[3] The loss of strength of Si upon yielding, which under ambient conditions has a diamondlike structure, is similar to recent observations on shock-compressed diamond samples.[21]

While the [100] and [111] orientations have different sound speeds under elastic compression, the comparable velocities after yielding suggest a more isotropic deformation response, consistent with the observations in Fig. 4(b). This anisotropic to isotropic material response during relaxation suggests a mechanism that rapidly reorganizes the single crystal such as twinning or the formation of dislocation cells.

In a recent study,[27] a 40-μm-thick Si [100] sample was uniaxially shock compressed to ~20 GPa over 4 ns, and ns x-ray diffraction techniques were used to determine the resultant change in lattice separation both normal and orthogonal to the shock front. In these experiments, measureable distortion of the unit cell normal to the shock front and a lack of measurable distortion of the unit cell orthogonal to the shock front was presented as "firm evidence that the response of single-crystal silicon to nanosecond time scale uniaxial shock compression along the (400) axis is anomalous in that it is purely elastic."[27] In order to explain this lack of plasticity, the authors used calculations at 0.1 GPa to infer dislocation velocities at 20 GPa of 0.1 mm s^{-1} and a resultant time scale of 10 ms to achieve a plastic strain of 5%. In those experiments, the input stress was not well defined, and no velocity wave profile or sound speed measurements were made. In contrast to the conclusions of those experiments, our wave profile and sound speed data [Secs. III B and III C] show conclusively that indeed plasticity in Si does occur rapidly over ns timescales.

The velocity pullback or ramp-down features in Fig. 5 (red arrows) are found to have a C_L consistent with an elastic response (red arrows in Fig. 6). This observation is seemingly at odds with the plastic-flow data reported in Sec. III B and Fig. 4, where it was established that the rate of stress relaxation after the precursor peak is consistent with the onset of plastic flow. Our interpretation of our data is this: At the loading surface, the precursor velocity rise is predominantly elastic. A rapid rise in the mobile dislocation density results in a rapid relaxation of the shear stress facilitated by the onset of plastic flow. Consequently, the rate of plastic flow is directly related to the stress relaxation rate after the peak elastic stress. Away from the loading surface the elastic precursor moves with a velocity of ~8.5 km/s (Si [100]), whereas the inelastic wave speed is ~5.7 km/s so there is a natural decoupling of the elastic and plastic waves. In this fashion, the velocity pullback associated with the precursor becomes predominantly elastic even though it was shaped initially through plasticity.

D. Strain-rate effects

In Fig. 7, the longitudinal elastic stress, σ_E, versus the strain rate at the onset of plastic deformation, $\dot{\varepsilon}_{pl}$, for Si [100] is shown. σ_E is calculated at the minimum pullback velocity of the elastic precursor [point 'a' in Fig. 5(a)] and $\dot{\varepsilon}_{pl}$ is defined at the base of the plastic wave (Fig. 5) and calculated through Eq. (1). In a recent study on ductile metals Al and Fe, it was observed that $\dot{\varepsilon}_{pl}$ was well correlated with the elastic stress,

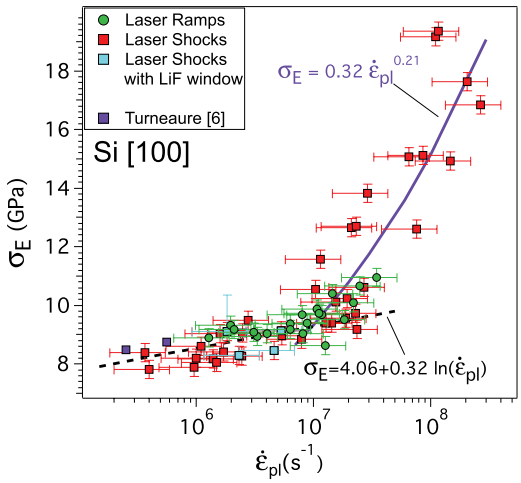

FIG. 7. (Color online) Elastic stress for Si [100] as a function of the strain rate at the onset of inelastic deformation. A two-regime fit to the data is observed. At strain rates less than ~10^7 s^{-1}, a $\sigma_E \propto \ln \dot{\varepsilon}_{pl}$ fit to the data is characteristic of a thermally activated dislocation flow, whereas at higher strain rates, a $\sigma_E \propto \ln \dot{\varepsilon}_{pl}^n$ fit characteristic of a phonon drag regime is observed.

σ_E, in the precursor wave for both shock- and ramp-wave compression.[10]

A number of phenomenological constitutive models have been developed to describe the $\sigma - \dot{\varepsilon}$ relationship in metals.[28] A general form of these models predicts a $\sigma \propto \ln(\dot{\varepsilon})$ dependency in the thermally activated dislocation flow regime with a transition to a $\sigma \propto \ln(\dot{\varepsilon})^n$ response in the high strain-rate phonon drag regime,[29] where $n < 1$ suggests an increase in saturation dislocation density with increasing strain rate.[30] In our data on Si [100], a covalent solid, we also observe two distinct strain-rate regimes. The data in Fig. 7 reveals a relative insensitivity of σ_E with strain rate for $\dot{\varepsilon}_{pl} \sim 10^5$–$10^7$ s^{-1}. At $\dot{\varepsilon}_{pl} > \sim 10^7$ s^{-1}, there is a marked increase in σ_E scaling with $\dot{\varepsilon}_{pl}$. A fit to the low strain-rate data, shown as the dashed curve in Fig. 7, is represented by

$$\sigma_E = 4.06 + 0.32 \ln(\dot{\varepsilon}_{pl}), \tag{2}$$

which is consistent with thermally activated dislocation flow facilitating the onset of significant plasticity.

For $\dot{\varepsilon}_{pl} > \sim 1 \times 10^7$ s^{-1}, σ_E increases sharply with $\dot{\varepsilon}_{pl}$. The sudden change in material response is consistent with high $\dot{\varepsilon}$ predictions for metals where dislocation velocities become limited by energy dissipation from interaction with lattice vibrations (phonon drag). A fit to the high strain-rate data, shown as the solid line in Fig. 7, is represented by

$$\sigma_E = 0.32 \dot{\varepsilon}_{pl}^{0.21 \pm 0.02}. \tag{3}$$

The data in Fig. 7 are consistent with a change in the dislocation flow mechanism from thermally activated to phonon drag in Si [100] at $\sigma_E \sim 9.3$ GPa and $\dot{\varepsilon}_{pl} \sim 10^7$ s^{-1}. This is the first time $\sigma_E - \dot{\varepsilon}_{pl}$ onset for phonon drag-dominated dislocation flow has been observed in a brittle and covalent semiconductor: previously such behavior has only been observed in ductile metals.

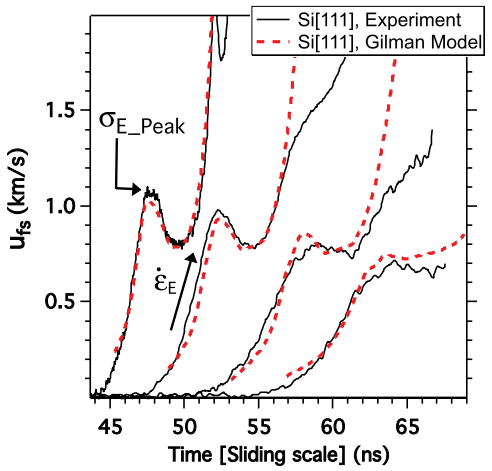

FIG. 8. (Color online) Four experiments in which 70-μm-thick Si [111] samples were ramp compressed with different loading strain rates (black curves) are modeled with the Gilman dislocation-based continuum model of plasticity (dashed curves). The trends of lower peak elastic stress, $\sigma_{\mathrm{E\_Peak}}$, with loading strain rate, $\dot{\varepsilon}_E$, are consistent with observations for Si [100] [Fig. 4(a)] and are well reproduced by the Gilman model.

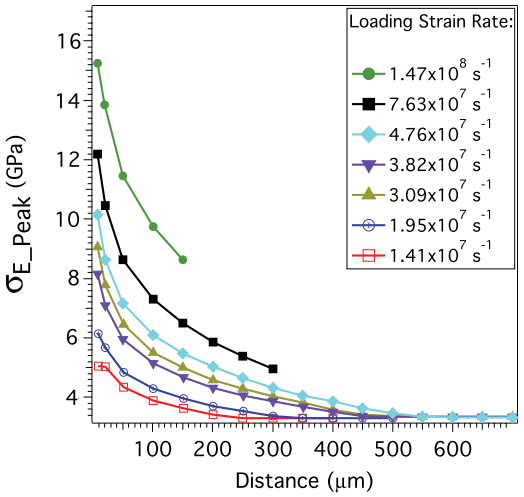

FIG. 9. (Color online) Peak elastic stress versus distance for Si as calculated from a Gilman model of plasticity for a range of initial strain rates. The elastic stress at the loading surface is a function of the loading strain rate. The rate of decay toward the steady state HEL is also dependent on the peak elastic stress at the loading surface [consistent with Fig. 3(a) inset].

IV. RATE-DEPENDENT PLASTICITY MODEL

To investigate further how the observations described in Sec. III are related to the kinetics of plastic flow, we consider a widely used rate-dependent, dislocation-based continuum model of plasticity. The hydrodynamic simulations of the Si $u(t)$ profiles shown here are based on the Gilman phenomenological model of plasticity.[31] The algorithm used for its implementation is due to Wilkins[32] and is described in Steinberg and Lund.[33] A full description of the model and input parameters may be found in Appendix B. The Gilman model was established in the late sixties and has been widely used in the intervening years to interpret time-dependent deformation data over a range of experimental platforms, materials, and deformation timescales.[11,12,34–36]

In Fig. 8, we apply the Gilman dislocation kinetics model to $u_{\mathrm{fs}}(t)$ profiles from four separate RWL experiments on 70-μm-thick Si [111] samples. The common input parameters for all the model fits (dashed curves) are described in Appendix B and Table I. The only fit-to-fit variable used to match the data was the loading strain rate, $\dot{\varepsilon}_E$. The data and the Gilman for Si [111] show the dependency of peak elastic stress with $\dot{\varepsilon}_E$ [similar to the Si [100] data in Fig. 4(a)]. We note that a remarkably good fit to the data can be attained but only if the initial dislocation density is assumed to be $\sim 10^9$ cm^{-2} or four orders of magnitude higher than the actual value as measured by TEM. Similar analysis on high-$\dot{\varepsilon}$ deformation of single crystal Cu,[37] W,[37] NaCl,[37] and LiF[12,34–37] have also shown that the requisite number of dislocations (to match experimental observations) exceed those available before compression by $\sim$3–4 orders of magnitude. In modeling our $u_{\mathrm{fs}}(t)$ profiles, this discrepancy poses a significant theoretical challenge: there are insufficient sources to accommodate shear stress relaxation at the $\sim 10^6$–10^8 s^{-1} strain rates associated with our experimental data. Without the requisite dislocation sources, a mechanism other than homogeneous dislocation flow must cause the u_{fs} precursor peak and subsequent stress relaxation. Some possibilities are twinning, shear localization, and fracture, or an unconventional dislocation nucleation mechanism to seed the initial density. Indeed, the conditions within our experiments, high strain rates, low temperatures, and a low density of dislocation nucleation centers, are all expected to be favorable towards twinning in Si.[14] Although we are not yet able to determine conclusively what deformation mechanism occurs in our experiment, we note that the trends in our data are well captured by applying the Gilman model.

TABLE I. Parameters used in rate-dependent model.

b (cm)	2.5×10^{-8}
υ_0(cm/μs)	0.9
N_0 (cm^{-2})	1.2×10^9
M (cm^{-2})	1.75×10^{11}
D (Mbar)	0.1
H (Mbar)	0.1

In Fig. 9, we plot the output of simulations for Si in which the peak elastic stress, $\sigma_{\mathrm{E\_Peak}}$, is plotted as a function of propagation distance for a range of loading strain rates [equivalent to $\dot{\varepsilon}_E$ in Fig. 2(c)]. The simulations reproduce the experimentally observed strain-rate behavior plotted in Figs. 3 and 4: (i) At a fixed distance near the loading surface, $\sigma_{\mathrm{E\_Peak}}$ increases as a function of strain rate [Fig. 3(a) inset and Fig. 4(a)]; (ii) the elastic stress decays in time from a peak value at the loading surface to a steady-state HEL surface at late times. These trends may be attributed to the high shear stresses that develop to multiply and move the dislocations.

The simulated bulk particle velocity time histories (blue) are shown for different Lagrangian positions in Fig. 10. The ratio of plastic strain ε_p to the overall strain $(1 - \rho_0/\rho)$ versus time for the corresponding Lagrangian positions are superimposed in red. At 5 μm away from the loading surface, the onset of plastic strain corresponds with the peak of the elastic precursor.

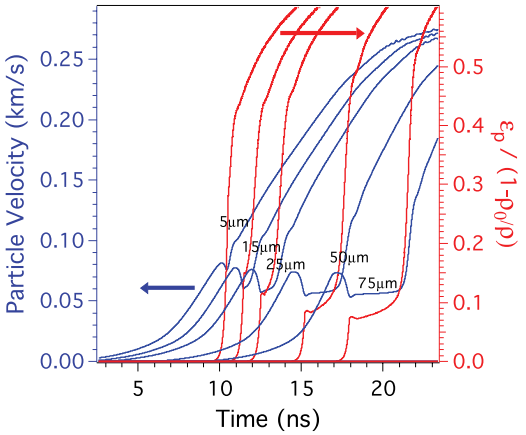

FIG. 10. (Color online) Evolution of elastic precursor in Si as a function of time and space, as calculated by the Gilman model. Each $u(t)$ profile (blue curves) are labeled by the corresponding distance into the Si sample. For each velocity profile, the plastic strain is shown as a red curve. For these simulations an initial dislocation density of 10^7 cm^{-2} and a loading strain rate of 2.5×10^8 s^{-1} were used as inputs.

Here the rate of stress relaxation after the precursor peak is shaped by the rate of plastic flow (seen experimentally in Fig. 4). Further into the bulk of the Si sample, the plastic strain decouples from the precursor and the precursor becomes predominantly elastic, which is consistent with the Lagrangian sound speed measurements reported in Fig. 6. The sequence demonstrates that the faster predominent elastic parts of the wave tend to run ahead of the parts of the wave having higher plastic strain contributions.

V. CONCLUSIONS

We have presented an experimental platform for exploring poorly understood plasticity effects in strain-rate regimes intermediate to those accessible with traditional dynamic deformation techniques of flyer-plate impact and split-Hopkinson pressure bar. Measuring material response while systematically varying the compression rate allows for new observations related to high strain-rate deformation to be made.

From the experimental data and modeling of plasticity presented in this paper we make the following conclusions.

(1) The elastic stress in single-crystal Si exhibits a strong rate- and orientation-dependence with values close to the loading surface exceeding twice those associated with the steady-state HEL (Fig. 3). Under shock compression, the Si [100] elastic precursor decays to the HEL yield surface (8.69 ± 0.63 GPa) after 100 μm or 11.7 ns of propagation. By contrast, Si [110], [111] elastic precursor decay continues out to 10-mm thicknesses with associated propagation times >1 μ sec to stresses of 4–5 GPa without reaching a steady-state yield surface. Further evidence of orientation-dependent dislocation flow is observed through differences within the precursor temporal shapes for Si [100] and [111] (Fig. 5).

(2) The data imply an orientation-*dependent* onset of plasticity (Fig. 3) and a subsequent orientation-*independent* relaxation (Figs. 4 and 6).

(3) At the loading surface, the peak elastic stress is a function of the loading strain rate. Plastic flow occurs at a rate exponentially dependent on the peak elastic stress (Figs. 4, 8, and 9).

(4) The precursor velocity pullback is temporally shaped through time-dependent plastic flow at the loading surface [Sec. III B]; however, at later times, Lagrangian sound speed measurements indicate that the precursor rise and pullback become fully elastic [Sec. III C]. This is consistent with a temporal decoupling of the elastic and plastic deformation fronts away from the loading surface. This picture is supported by predictions from the phenomenological plasticity model in Sec. IV (Fig. 10).

(5) We observe correlation between the elastic stress at the onset of plastic deformation, σ_E, and the strain rate at the onset of plastic deformation, $\dot{\varepsilon}_{pl}$. At strain rates above $\sim 10^7$ s^{-1}, there is a rapid increase in the measured elastic stress consistent with a transition from dislocation flow mediated by thermal activation to a phonon drag regime. This is consistent with recent observations in Fe and Al.[10]

ACKNOWLEDGMENTS

We thank Stefan Turneaure for providing the raw velocity data from experiments at Washington State University for analysis within this paper. We also thank Stephanie Uhlich, Julie Hamilton, and Walter Unites for help in the target preparation. This work was performed under the auspices of the US Department of Energy by Lawrence Livermore National Laboratory under Contract No. DE-AC52-07NA27344.

APPENDIX A: DEFINITION OF STRAIN RATE [EQ. (1)]

Zel'dovitch and Raizer[38] give conservation of mass in Lagrangian coordinates as

$$\frac{\partial V}{\partial t} = V_0 \frac{\partial u}{\partial h} \tag{A1}$$

Consider an infinitesimally small shock at Lagrangian position $h_s(t)$—so small that virtually no entropy is introduced—traveling at the Lagrangian sound speed C_L. We integrate over a region that encompasses this small shock, $h_1 \to h_2$.

$$\frac{\partial}{\partial t}\left(\int_{h_1}^{h_s(t)} V dh + \int_{h_s(t)}^{h_2} V dh\right) = V_0 \int_{u_1}^{u_2} du \tag{A2}$$

$$\frac{\partial}{\partial t}[V_1(h_s(t) - h_1) + V_2(h_2 - h_s(t))] = V_0(u_2 - u_1) \tag{A3}$$

$$C_L(V_1 - V_2) = V_0(u_2 - u_1). \tag{A4}$$

Define the strain as $\varepsilon \equiv \ln V \Rightarrow \Delta\varepsilon = \frac{\Delta V}{V}$, so that

$$\Delta\varepsilon = \frac{V_0}{V}\frac{\Delta u}{C_L}. \tag{A5}$$

Finally, assume a continuous ramp composed of a series of these small shocks and divide by a small time, Δt,

$$\frac{\Delta\varepsilon}{\Delta t} \to \left.\frac{\partial\varepsilon}{\partial t}\right|_h = \frac{V_0}{V}\frac{\partial u/\partial t|_h}{C_L} \tag{A6}$$

$$\dot{\varepsilon} = \frac{V_0}{V}\frac{\dot{u}}{C_L}. \tag{A7}$$

At low levels of compression $\frac{V_0}{V} \approx 1$ and $\dot{\varepsilon} \approx \frac{\dot{u}}{C_L}$.

APPENDIX B: RATE-DEPENDENT PLASTICITY MODEL

1. Gilman model of rate-dependent plasticity

Detailed below is a description of the rate-dependent plasticity model discussed in Sec. IV. The longitudinal stress σ_1, the pressure p, and the deviatoric stress s_1 are related by

$$\sigma_j = -p + s_j. \tag{B1}$$

where $j = 1, 2,$ or 3. The components of the deviatoric stresses for the Von Mises yield criterion satisfy

$$s_1 + s_2 + s_3 = 0, \tag{B2}$$

and

$$s_1^2 + s_2^2 + s_3^2 = \tfrac{2}{3}Y, \tag{B3}$$

where Y is the yield stress. The components transverse to the longitudinal shock direction are assumed to be equal: $s_2 = s_3$. The components of the plastic strain (ε_j^p) obey the nondilatational (no opening of voids) condition,

$$\varepsilon_1^p + \varepsilon_2^p + \varepsilon_3^p = 0. \tag{B4}$$

In the one-dimensional simulations, the total velocity gradient $d\Theta/dt$, or strain rate, is the sum of the elastic strain rate, with shear modulus G and the plastic strain rate

$$\dot{\varepsilon}_j^p = \dot{\Theta}_j - \dot{s}_j \frac{1}{2G}. \tag{B5}$$

The stress deviators are updated in the finite difference code according to the expressions involving the equivalent plastic strain ε_p,

$$\dot{s}_j = 2G\left(\dot{\Theta}_j - \dot{\varepsilon}_p \frac{s_j}{2/3Y}\right), \quad \frac{2}{3}\dot{\varepsilon}_p^2 = \left(\dot{\varepsilon}_1^2\right)^2 + \left(\dot{\varepsilon}_2^2\right)^2 + \left(\dot{\varepsilon}_3^2\right)^2. \tag{B6}$$

In the current simulations, we use the Gilman expression for the plastic strain rate,

$$\dot{\varepsilon}_P = b(N_0 + M\varepsilon_P)\nu_0 e^{-\frac{H\varepsilon_P + D}{Y}}, \tag{B7}$$

where N_0 is the initial mobile dislocation density, M is proportional to the logarithmic multiplication of the dislocation density, D is background drag stress, ν_0 is the shear wave speed, and H is an additional drag stress.

2. Summary of hydrodynamic simulations of Si with gilman model

The rate-dependent Gilman model is activated in the simulation when the deviatoric stress exceeds a specified value, typically the orientation-dependent HEL. The plastic strain rate for a given computational time step is determined self-consistently from the updated deviatoric stress, the plastic strain, and the Von Mises yield condition. Specifically, the computed deviatoric stress for a specific time step is relaxed due to plastic flow using the relation,

$$s_j = \frac{\hat{s}_j}{1 + [3G/Y(\dot{\varepsilon}_p')]\dot{\varepsilon}_p'}. \tag{B8}$$

The prime on the plastic strain rate denotes the value at the end of the time step. The Von Mises constraint allows the effective yield stress Y to be self-consistently evaluated by solving the nonlinear equation,

$$\dot{\varepsilon}_p'(Y) = \frac{1}{3G\delta t}\left(\sqrt{\frac{3}{2}}|\hat{s}| - Y\right), \quad |\hat{s}_j| = \hat{s}_1^2 + \hat{s}_2^2 + \hat{s}_3^2. \tag{B9}$$

Once Y is evaluated, the plastic strain rate is determined from Eq. (B7), and the new plastic strain is incremented. Representative simulations for Si (Figs. 9 and 10) were performed using the Gilman parameters summarized in Table I and assuming a HEL of 3.3 GPa. The value for ν_0 representing the maximum dislocation velocity is higher than the shear velocity expected for Si. The initial dislocation density, $N_0 = 10^9$ cm^{-2} used in the simulations, is high compared to the measured Si preshot samples.

---

*Current address: University of Washington, Seattle, Washington, USA.

[1] M. Itoh, M. Katayama, and R. Rainsberger, Mater. Sci. Forum **465**, 73 (2004).

[2] S. W. Haan, P. A. Amendt, T. R. Dittrich, B. A. Hammel, S. P. Hatchett, M. C. Herrmann, O. A. Hurricane, O. S. Jones, J. D. Lindl, M. M. Marinak, D. Munro, S. M. Pollaine, J. D. Salmonson, G. L. Strobel, and L. J. Suter, Nucl. Fusion **44**, S171 (2004).

[3] T. Goto, T. Sato, and Y. Syono, Jpn. J. Appl. Phys. **21**, L369 (1982).

[4] W. H. Gust and E. B. Royce, J. Appl. Phys. **42**, 1897 (1971).

[5] S. J. Turneaure and Y. M. Gupta, Appl. Phys. Lett. **91**, 201913 (2007).

[6] M. N. Pavlovskii, Sov. Phys. Solid State **9**, 2514 (1968).

[7] P. P. Gillis and J. J. Gilman, J. Appl. Phys. **36**, 3380 (1965).

[8] E. M. Bringa, A. Caro, Y. Wang, M. Victoria, J. M. McNaney, B. A. Remington, R. F. Smith, B. R. Torralva, and H. Van Swygenhoven, Science **309**, 1838 (2005).

[9] J. E. Field, S. M. Walley, W. G. Proud, H. T. Goldrein, and C. R. Siviour, Int. J. Imp. Eng. **30**, 725 (2004).

[10] R. F. Smith, J. H. Eggert, R. E. Rudd, D. C. Swift, C. A. Bolme, and G. W. Collins, J. Appl. Phys. **110**, 123515 (2011).

[11] A. S. Argon, *Strengthening Mechanisms in Crystal Plasticity* (Oxford University Press, Oxford, 2008).

[12] B. J. Jensen and Y. M. Gupta, J. Appl. Phys. **104**, 013510 (2008)

[13] M. I. McMahon, R. J. Nelmes, N. G. Wright, and D. R. Allan, Phys. Rev. B **50**, 739 (1994).

[14] P. Pirouz, Scr. Metall. **21**, 1463 (1987); K. Yasutake, S. Shimizu, M. Umeno, H. Kawabe, J. Appl. Phys. **61**, 940 (1987).

[15] S. D. Gilev and A. M. Trubachev, J. Phys.: Condens. Matter **16**, 8139 (2004).

[16] J. Tirosh and O. Abraham, Mech. Mater. **39**, 760 (2007).

[17] Previous studies of brittle materials under shock compression (Refs. 39 and 40) have suggested that brittle-failure waves, which

lag behind the compressive wave, are a potential mechanism for relieving large shear strains (Ref. 39). However, although failure waves have been observed in a number of different materials, they have not been observed in studies of shock compressed Si (Ref. 40). Those results and the characteristic time lag between compression and failure waves suggest that failure waves are not relevant to our observations.

[18]R. F. Smith, J. H. Eggert, M. D. Saculla, A. F. Jankowski, M. Bastea, D. G. Hicks, and G. W. Collins, Phys. Rev. Lett. **101**, 065701 (2008).

[19]R. F. Smith, J. H. Eggert, A. Jankowski, P. M. Celliers, M. J. Edwards, Y. M. Gupta, J. R. Asay, and G. W. Collins, Phys. Rev. Lett. **98**, 065701 (2007).

[20]T. R. Boehly, D. L. Brown, R. S. Craxton, R. L. Keck, J. P. Knauer, J. H. Kelly, T. J. Kessler, S. A. Kumpan, S. J. Loucks, S. A. Letzring, F. J. Marshall, R. L. McCrory, S. F. B. Morse, W. Seka, J. M. Soures, and C. P. Verdon, Opt. Commun. **133**, 495 (1997)

[21]R. S. McWilliams, J. H. Eggert, D. G. Hicks, D. K. Bradley, P. M. Celliers, D. K. Spaulding, T. R. Boehly, G. W. Collins, and R. Jeanloz, Phys. Rev. B **81**, 014111 (2010).

[22]R. F. Smith, S. M. Pollaine, S. J. Moon, K. T. Lorenz, P. M. Celliers, J. H. Eggert, H.-S. Park, and G. W. Collins, Phys. Plas. **14**, 057105 (2007).

[23]P. M. Celliers, D. K. Bradley, G. W. Collins, D. G. Hicks, T. R. Boehly, and W. J. Armstrong, Rev. Sci. Instrum. **75**, 4916 (2004).

[24]H. J. McSkimin and P. Andreatch, J. Appl. Phys. **35**, 2161 (1964); **35**, 3312 (1964).

[25]J. R. Asay, T. Ao, T. J. Vogler, J.-P. Davis, and G. T. Gray III, J. Appl. Phys. **106**, 073515 (2009).

[26]S. D. Rothman, J.-P. Davis, J. Maw, C. M. Robinson, K. Parker, and J. Palmer, J. Phys. D **38**, 733 (2005).

[27]A. Loveridge-Smith, A. Allen, J. Belak, T. Boehly, A. Hauer, B. Holian, D. Kalantar, G. Kyrala, R. W. Lee, P. Lomdahl, M. A. Meyers, D. Paisley, S. Pollaine, B. Remington, D. C. Swift, S. Weber, and J. S. Wark, Phys. Rev. Lett. **86**, 2349 (2001).

[28]B. A. Remington, P. Allen, E. M. Bringa, J. Hawreliak, D. Ho, K. T. Lorenz, H. Lorenzana, J. M. McNaney, M. A. Meyers, S. W. Pollaine, K. Rosolankova, B. Sadik, M. S. Schneider, D. Swift, J. Wark, and B. Yaakobi, Mater. Sci. Tech. **22**, 474 (2006).

[29]K. Sakino, J. Phys. IV **10**(9), 57 (2000).

[30]N. R. Barton, J. V. Bernier, R. Becker, A. Arsenlis, R. Cavallo, J. Marian, M. Rhee, H.-S. Park, B. A. Remington, and R. T. Olson, J. Appl. Phys. **109**, 073501 (2009).

[31]J. J. Gilman, *Micromechanics of Flow in Solids* (McGraw-Hill, New York, 1969).

[32]Mark L. Wilkins, *Calculation of Elastic-Plastic Flow*, Rept. UCRL-7322 Rev. 1, Lawrence Livermore Laboratory (1969).

[33]D. J. Steinberg and M. J. Lund, J. Appl. Phys. **65**, 1528 (1989).

[34]J. R. Asay, G. R. Fowles, G. E. Durall, M. H. Miles, and R. F. Tinder, J. Appl. Phys. **43**, 2132 (1972).

[35]T. E. Arvidsson, Y. M. Gupta, and G. E. Duvall, J. Appl. Phys. **46**, 4474 (1975).

[36]Y. M. Gupta, G. E. Duvall, and G. R. Fowles, J. Appl. Phys. **46**, 532 (1975).

[37]J. N. Johnson, O. E. Jones, and T. E. Michaels, J. Appl. Phys. **41**, 2330 (1970).

[38]Y. B. Zel'dovich and Y. P. Raiser, Eq. 1.19 in *Physics of Shock Waves and High-Temperature Hydrodynamic Phenomena* (Courier Dover Publications, New York, 2002).

[39]D. E. Grady, J. Geo. Res. **85**, 913 (1980).

[40]G. I. Kanel, A. A. Bogach, S. V. Razorenov, A. S. Savinykh, Z. Chen, and A. Rajendran, *Shock Compression of Condensed Matter—2003*, edited by M. D. Furnish *et al.*, AIP Conf. Proc. 706 (AIP, Melville, NY, 2004), pp. 739–742.